# Localized ultra-low velocity zones at the eastern boundary of Pacific LLSVP

**Article** *in* Earth and Planetary Science Letters · February 2019

DOI: 10.1016/j.epsl.2018.11.037

CITATIONS
3

READS
152

**3 authors**, including:

Xiaolong Ma
Chinese Academy of Sciences
**4** PUBLICATIONS **13** CITATIONS
SEE PROFILE

Xinlei Sun
Gungzhou Institute of Geochemistry Chinese Academy of Sciences
**39** PUBLICATIONS **471** CITATIONS
SEE PROFILE

Earth and Planetary Science Letters 507 (2019) 40–49

Contents lists available at ScienceDirect

Earth and Planetary Science Letters

www.elsevier.com/locate/epsl

# Localized ultra-low velocity zones at the eastern boundary of Pacific LLSVP

Xiaolong Ma [a,b,c], Xinlei Sun [a,*], Christine Thomas [c]

[a] State Key Laboratory of Isotope Geochemistry, Guangzhou Institute of Geochemistry, Chinese Academy of Sciences, Guangzhou 510640, China
[b] University of Chinese Academy of Sciences, Beijing 10069, China
[c] Institut für Geophysik, Westfälische Wilhelms-Universität Münster, Münster 48149, Germany

ARTICLE INFO

*Article history:*
Received 17 May 2018
Received in revised form 19 November 2018
Accepted 24 November 2018
Available online xxxx
Editor: M. Ishii

*Keywords:*
core–mantle boundary
ultra-low velocity zone
compositional heterogeneity
PKP precursor

ABSTRACT

It is suggested that ultra-low velocity zones (ULVZs) are often located near the boundary of large low shear velocity zones (LLSVPs). Previous studies have provided evidence of ULVZs residing along the western and northern boundary of the Pacific LLSVP. However, so far there is no detailed report on ULVZs along the eastern boundary of the Pacific LLSVP. In this study, we collected PKP precursor waveforms from earthquakes in South America that are recorded by seismic arrays in Australia. These precursors show clear and coherent phases. Slowness and migration analysis of these precursors indicate that they originate from scatterers in the lowermost mantle east of the Pacific LLSVP. Waveform modeling suggests that these seismic scatterers are localized ULVZs, with P-wave velocity reductions of ~3–10% and thickness of several tens of kilometers. The dimension of the ULVZs and the geological correlation of the ULVZs with the Galapagos hotspot, suggest that these ULVZs are mainly due to compositionally distinct heterogeneities, although partial melting cannot be completely ruled out. The distribution of both coherent and incoherent PKP precursors also suggests vigorous small-scale mantle convections near the edges of the LLSVP.



## 1. Introduction

The lowermost mantle is identified as a complex region exhibiting strong, multi-scale heterogeneities (e.g., Lay and Garnero, 2011). During the last decade, seismic tomography has consistently revealed large-scale heterogeneous structures in the deep mantle, such as large low shear velocity provinces (LLSVPs) beneath the African continent and the central Pacific as well as high velocity anomalies surrounding the Pacific Ocean (e.g., Simmons et al., 2010). At the same time, small-scale heterogeneities, such as ultra-low velocity zones (ULVZs), are also detected by various studies (see reviews by Yu and Garnero, 2018). These small-scale structures are believed to be related to thermo-chemical processes near the core–mantle boundary (CMB), and thus provide detailed information on dynamic processes in the lowermost mantle (Lay and Garnero, 2011; Tackley, 2012).

ULVZs are seismic anomalies at the base of Earth's mantle. They exhibit large compressional and shear velocity reductions (up to 10% and 30%, respectively) as well as density increases (up to 5–10%) (e.g., Garnero and Helmberger, 1998; Rost et al., 2006). The thicknesses of ULVZs vary from several km to ~100 km (Thorne and Garnero, 2004; Zhao et al., 2017), and the lateral dimensions of ULVZs are from tens of km (Wen and Helmberger, 1998; Rost et al., 2005) to ~900 km (Cottaar and Romanowicz, 2012; Thorne et al., 2013; Yuan and Romanowicz, 2017). Seismological studies have revealed that ULVZs are not uniformly distributed at the CMB. Instead, most of them reside near the boundary of LLSVP (McNamara et al., 2010; Yu and Garnero, 2018), or are associated with subducted slabs (Yao and Wen, 2014). The location of ULVZs is also suggested to correlate with the surface locations of hotspots, although this is not well constrained (Williams et al., 1998; Garnero et al., 2016).

Various mechanisms for ULVZ's origin have been proposed, which essentially emphasize distinct thermal and compositional anomalies. It is believed that partial melting in the lowermost mantle may explain the 3:1 velocity reduction ratio in shear and compressional waves of ULVZs (Williams and Garnero, 1996; Berryman, 2000). However, the hottest regions in the lowermost mantle are commonly located inside the LLSVPs (Li et al., 2017), partial melting thus has difficulty in explaining ULVZs along the boundaries. On the other hand, geodynamic modeling has demonstrated that dense ULVZs may preferentially reside at the boundary of LLSVP due to deep-mantle convection (Hernlund and Tackley, 2007; McNamara et al., 2010), supporting a compositionally dis-

* Corresponding author.
*E-mail address:* xsun@gig.ac.cn (X. Sun).

https://doi.org/10.1016/j.epsl.2018.11.037
0012-821X/

tinct origin for most ULVZs (Li et al., 2017). Nevertheless, the dynamic process and the thermal/chemical state at the base of the mantle may generate different ULVZs. In return, the distribution, geometry and physical properties of the ULVZs can also provide information on the CMB dynamics and compositions. Thus a more complete picture of ULVZs is important and highly needed.

Among various seismic probes of ULVZ, S waves diffraction and reflections (e.g., Rost et al., 2006; Cottaar and Romanowicz, 2012; Yuan and Romanowicz, 2017; Zhao et al., 2017) are most common, because ULVZs generally have larger S-wave variations. P-wave studies include precursor and/or postcursor of PcP and ScP synthetics (e.g., Mori and Helmberger, 1995; Rost et al., 2006), PKP precursors energy or slowness modeling (e.g., Vidale and Hedlin, 1998; Vanacore et al., 2010) and PKP precursor waveform modeling (e.g., Wen and Helmberger, 1998; Thomas et al., 2009). These probes provide different constraints on ULVZ physical properties. Although there are uncertainties/trade offs in the results, the general features of ULVZ are consistent.

The Pacific is an ideal and often studied region for ULVZs. The deep-focus earthquakes and dense seismic stations distributed around the Circum-Pacific region provide abundant data sampling this region at the CMB. However, most of the currently resolved ULVZs in the Pacific are distributed near the western, northern/northeastern boundaries of the Pacific LLSVP, as well as in the central part of it (see McNamara et al., 2010; Yu and Garnero, 2018). Few studies have been carried out to detect ULVZs in eastern portions of the Pacific LLSVP. This is because that most phases used to detect ULVZs, e.g., SPdKS/SKPdS, Sdiff or precursors and postcursors of PcP/ScP/ScS, have difficulty in sampling the eastern part of the Pacific LLSVP for the current earthquake-station distributions.

In this study, we investigated another seismic signal, PKP precursors, to map ULVZs around the eastern Pacific LLSVP. The precursor waveforms are from earthquakes in South America and recorded by two dense seismic arrays deployed in central Australia. The waveforms present clear, coherent phases in high frequency content. Slowness analysis and waveform modeling suggest that the ULVZs near the eastern boundary of the Pacific LLSVP are isolated anomalies with a dimension of several tens of km in both thickness and width. These ULVZs may result from compositionally distinct materials, which may be introduced by the subducted slabs or due to the core–mantle interaction. The distribution and lateral dimensions of the ULVZs also imply complex small-scale mantle convections resulted from both active subductions and upwellings in the lowermost mantle.

## 2. Data

We searched for PKP precursors (Fig. 1) from seismic waveform data recorded by the seismic stations in Australia between the year 2005 and 2016. To obtain clear PKP precursors, we selected earthquakes with magnitude between 5.0 Mw and 7.1 Mw for ruling out complex source time functions and required the depths to be greater than 50 km for impulsive P waveforms. We also required the epicentral distances to be between 130° to 143°, at which the precursors are most obvious.

We noticed that among all the stations, the Warramunga Array (WRA) and Alice Spring Array (ASAR) stations have high quality PKP precursors and these precursors include clear phase-like waveforms that can be separated from later precursor wave trains. Other stations in our distance range generally have no obvious coherent PKP precursors. On the other hand, although earthquakes from the north and south side of our region show some PKP precursors too, the clear phase-like precursors are mostly observed from earthquakes concentrated on the central region. Thus in this paper, we focus only on the seismic data of the two arrays from

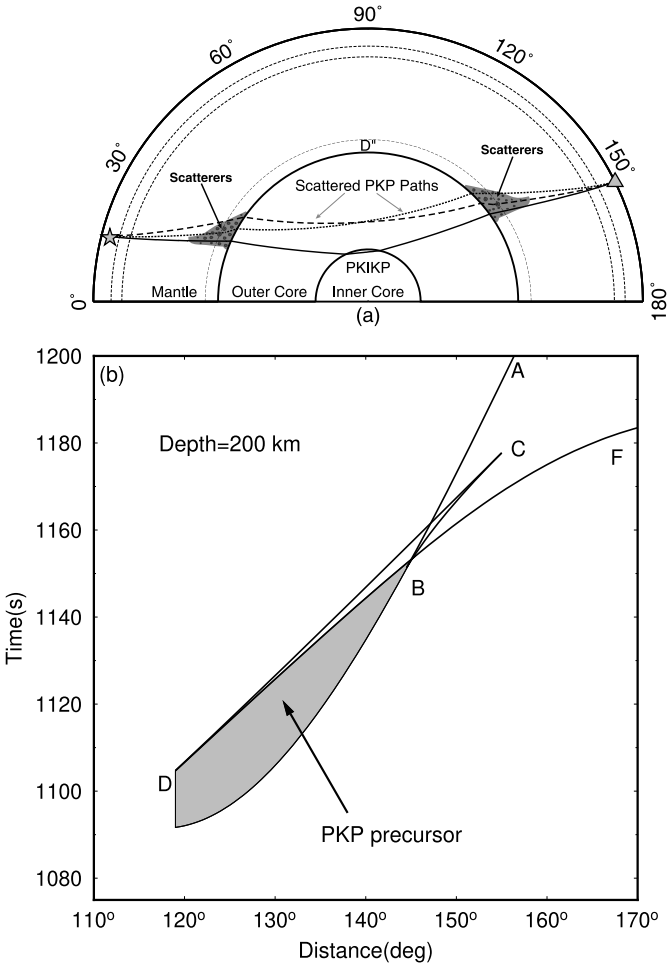


**Fig. 1.** (a) Ray-paths of PKIKP and scattered PKP waves. The PKP precursors are scattered waves generated by the seismic scatterers (black dots) in the lower mantle beneath the source or receiver. The star denotes the earthquake at the surface, and the triangle denotes the seismic station. (b) Travel time curves of four branches of PKP. Due to the unusual ray paths caused by scatterers in the lower mantle, the scattered waves can precede PKIKP by up to ~20 s. The shaded region indicates the earlier arrival times for precursors.

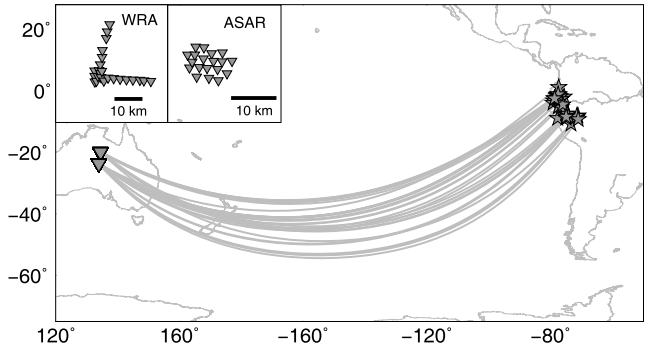


**Fig. 2.** Distribution of seismic stations (inverted triangles) and earthquakes (stars) in this study. Inserted boxes show the magnified areas for two seismic arrays (ASAR and WRA), respectively.

earthquakes in the central region. Finally 40 earthquakes are selected (Fig. 2) (Table S1).

WRA and ASAR both have small apertures and consist of 25 and 19 seismic stations, respectively (Fig. 2). The average distance between stations in these two arrays is about 3–5 km, thus making it well suited to study the high-frequency PKP precursor waveforms. After removing the instrument response and convolving

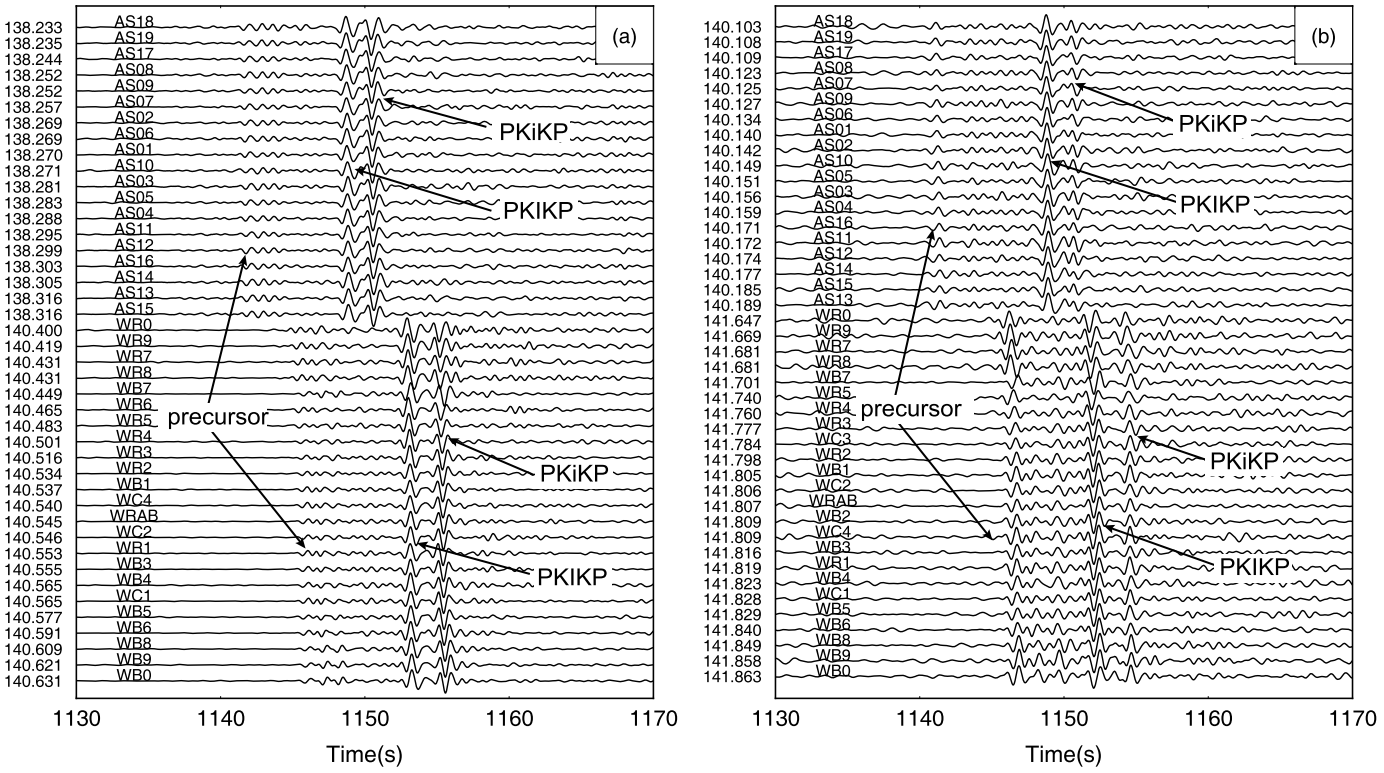


**Fig. 3.** Examples of waveforms that show (a) random precursors (type 1) and (b) clear coherent PKP precursors (type 2) recorded by two arrays, respectively.

with the WWSSN (World Wide Standard Seismic Network) short-period instrument response, we then applied a three-pole Butterworth band-pass filter to the seismograms with a frequency band between 0.5 Hz and 2.0 Hz to ensure good signal-to-noise ratios for both PKIKP phases and their precursors.

Based on the characteristics of the waveforms, we categorized the observed precursors into two types: one type of precursor is featured by continuous and random wave trains that cannot be separated from each other (Fig. 3a). We call them type 1 data. This type of precursor is generally analyzed based on the envelope (e.g., Hedlin et al., 1997; Mancinelli and Shearer, 2013). In contrast, another type of data shows clear, strong phase-like precursors (mostly first-arrival phases) that are distinguishable from later random precursors as mentioned above (type 2) (Fig. 3b). In some waveforms, the amplitudes of type 2 precursors are comparable to or larger than amplitudes of PKIKP phases. Although diffraction of PKP b-caustic waves can also be recorded as precursory signals in this distance range, it is impossible in our case, because diffracted waves are generally low-frequency ($<$0.2 Hz) signals (Thomas et al., 2009), while our precursors are visible in a high-frequency band. So the precursors are more likely scattered waves from small-scale heterogeneous structures in the lower mantle. In this study, we mainly focus on the special distinct precursors (type 2) and explore the structure causing them.

## 3. Location of seismic heterogeneities

The locations of scatterers are ambiguous because scattering from either the source side or receiver side (Fig. 1) can generate similar PKP precursors (e.g., Wen, 2000). However, the incident angles of PKP precursors scattered from these two sides are different, thus slowness can be used as a reference to locate the scatterers (Cao and Romanowicz, 2007; Miller and Niu, 2008). Using array processing method (Rost and Thomas, 2002), we measured the slowness and back-azimuth of PKP precursors for each event. After time shifts based on the slowness and back-azimuth of PKP precursors, all the seismograms are 3rd-root stacked for all combinations of slowness and back-azimuth in a prescribed range. Then the optimal slowness and back-azimuth are chosen when the stacked amplitude is maximum. An example of coherent PKP precursor and PKIKP with their slowness and back-azimuth information is shown in Fig. 4.

We applied this stacking technique to all coherent PKP precursors (type 2) and displayed the results in Fig. S1. The slowness values of these PKP precursors exhibit a wide range from 1.70 to 4.26 s/deg, and the back-azimuths span from about 114° to 145°. According to Cao and Romanowicz (2007) (Fig. 5 in their paper), scattered waves originating from the receiver side generally show slowness values less than 3.0 s/deg while those from the source side tend to show values larger than 3.0 s/deg. The wide range of slowness values indicates that the precursors are likely caused by scatterers located at both the source and receiver sides, namely beneath the eastern Pacific and southeast Australia, respectively.

Fig. 5 shows the entry and exit points of both PKIKP and PKP b-caustic waves through the CMB and comparisons with the boundary of Pacific LLSVP from regional studies (He and Wen, 2012; Frost and Rost, 2014). Although seismic scatterers are distributed on both sides, PKIKP and PKP b-caustic points are well separated on the source side with respect to the LLSVP location, with only PKP b-caustic piercing points interacting with the LLSVP. On the receiver side, both of the PKIKP and PKP b-caustic phases interact with the LLSVP. Moreover, the PKP b-caustic exit points of both type 1 and type 2 data are overlapping at the receiver side, but are separated at the source side. This indicates that the difference in precursors likely originates from the source side. We further found that most of the coherent large-amplitude precursors show slowness values larger than 3.0 s/deg, implying strong-scattering anomalies lie at the CMB beneath the source. Although there are scatterers on the receiver side, in the following text, we focus on the eastern side of the Pacific LLSVP, the source side at the CMB, as the data sampling in this region are of good quality.

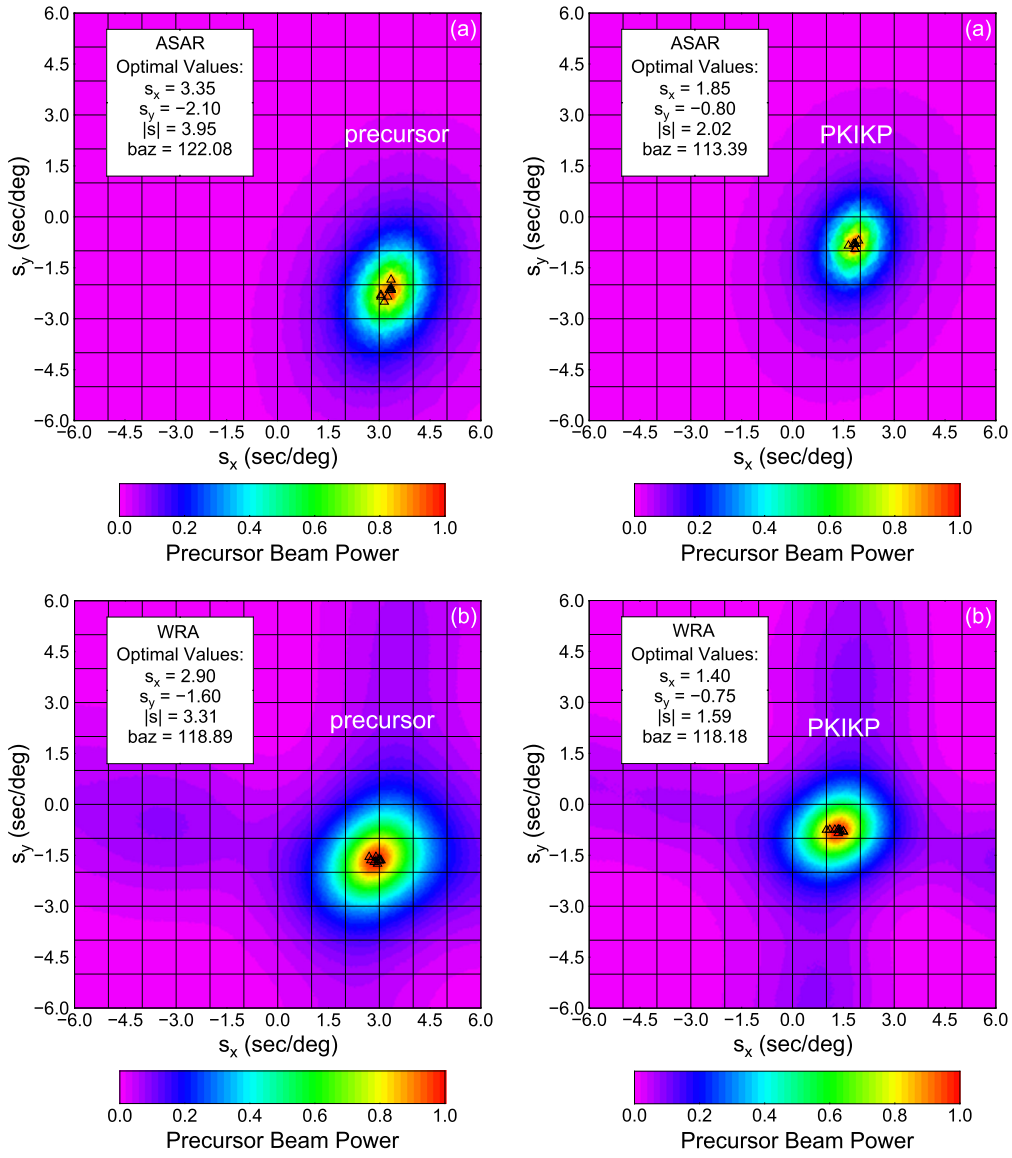


**Fig. 4.** Optimal slowness and back-azimuth estimations for the first-arrival PKP precursors and PKIKP shown in Fig. 3b. (a) and (b) are for ASAR and WRA arrays respectively. The beam power is normalized by the maximum amplitude value of the stacked precursors. The triangles represent an error measurement using a bootstrap technique.

To place tighter constraints on the spatial distribution of scatterers, we imaged the location of scatterers using a migration method (Thomas et al., 1999). In this process, we only chose coherent PKP precursors (type 2) with slowness larger than 3.0 s/deg, which means the scatterers are at the source side (east of the Pacific LLSVP). The possible scattering region is set up as a rectangular area that spans from 0°S to 30°S in latitude and from 75°W to 105°W in longitude in order to include all the entry points at the CMB in Fig. 5. The area is then divided into 5 layers from the CMB to 200 km above the CMB, with each layer further divided into 1.0° × 1.0° uniform grid of nodes. Each node is treated as a source of scatterer, and theoretical PKP precursor travel times are calculated by summing the two legs of the raypath. One leg is from the source to the scatterer node, and the other is from the scatterer node to the receiver. Then a 2 s window around the theoretical arrival time for this location was selected to compute the semblance coefficients (e.g., Kaneshima, 2013) for each potential scatterer. The area with high values of semblance coefficient represents the most likely place where strong seismic scatterers exist. We only show the semblance coefficient distributions at three depths near the CMB in Fig. 6, where localized strong heterogeneities are most likely to exist.

The whole scattering region is distributed from 2°S to 25°S in latitude, and between 80°W and 100°W in longitude. In addition, strong scatterers (blue color) are detected and located about 14–16° away from the center of the earthquake cluster, which generally correlate with the eastern boundary of the Pacific LLSVP detected from He and Wen (2012), Frost and Rost (2014). On the other hand, other scattering areas with weaker power imply lower abundance in small-scale heterogeneities or weak scattering. We notice that the strong scattering regions are not always connected, which may suggest that the distribution of these scatterers is quite complex.

## 4. Geometry and structure of localized ULVZ

To further constrain the size and the velocity variations of scatterers beneath the eastern Pacific LLSVP, we selected three type 2 events with slowness larger than 3.0 s/deg for waveform modeling (Table 1). These PKP precursors imply coherent scattering along the eastern LLSVP boundary, thus providing essential infor-

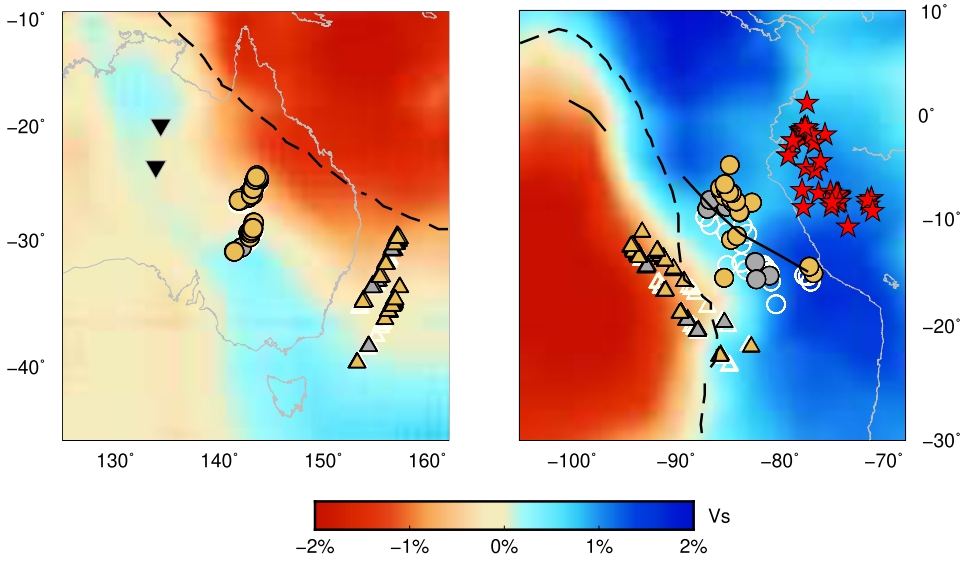


**Fig. 5.** The entry and exit points of PKIKP (circles) and PKP b-caustic (triangles) at the core–mantle boundary beneath the source and receiver side. The open white circles and triangles represent the piercing points of PKIKP and PKP b-caustic for random (type 1) precursor waveforms, respectively, while the solid ones represent the piercing points for coherent (type 2) precursor waveforms. Furthermore, we divide the type 2 precursors into source-side scattering (light brown) and receiver-side (gray) scattering. The background model is the S-wave mantle model for the lowest layer from GyPSuM (Simmons et al., 2010). Stars represent events that show all types of PKP precursors and inverted black triangles represent the two seismic arrays. The dashed line denotes the S-wave boundary of Pacific LLSVP from He and Wen (2012) while the solid line denotes the P-wave boundary from Frost and Rost (2014).

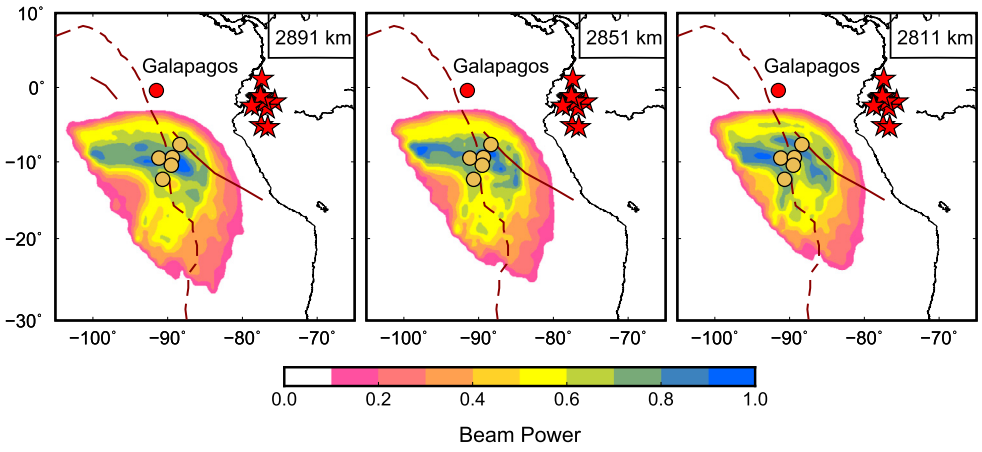


**Fig. 6.** Migration results showing scattering regions beneath the eastern Pacific Ocean for three different depths (2891 km, 2851 km and 2811 km) above the CMB. The red circle represents the Galapagos hot spot and the red stars represent earthquakes used for migration. The light brown circles denote the location of ULVZs inferred from the waveform modeling results, which is discussed later. The dashed and solid lines are the same as shown in Fig. 5.

**Table 1**
Events used for modeling.

| Events | Lat (°N) | Lon (°E) | Dep (km) | Slowness (s/deg) | | Back-azimuth (°) | |
|---|---|---|---|---|---|---|---|
| | | | | WRA | ASAR | WRA | ASAR |
| 2006.10.31.09.55 | −1.38° | −77.73° | 182.8 | 3.31 | 3.95 | 118.89 | 122.08 |
| 2007.07.21.18.58 | −1.52° | −77.95° | 169.1 | 3.06 | 3.79 | 122.11 | 123.69 |
| 2010.08.12.11.54 | −1.28° | −77.37° | 206.5 | 3.12 | xx | 121.90 | xx |

mation for the anomalous structures in this region. The measured back-azimuths of these precursors are roughly the same as the theoretical back-azimuths from stations to events (Table 1), suggesting that scattering generally occurs within the great-circle-path plane.

We computed the synthetic PKP precursors using the AxiSEM program, an axisymmetric spectral-element method for global wave propagation (Nissen-Meyer et al., 2014). The dominant period of the synthetics is 1.0–2.0 s, which is generally compatible with that of our short-period data (0.5 s–2.0 s). The moment tensor solutions for each event are obtained from the global CMT (Centroid Moment Tensor) catalog.

Different models are tested in order to better constrain the geometry and physical properties of the scattering heterogeneities. Fig. 7 shows that a 1D ULVZ model as well as long wavelength heterogeneous model cannot generate the type 2 PKP precursors in our data. In addition, random scatterers above the CMB can generate random precursors, similar as our type 1 data (Fig. S2). In order to generate type 2 PKP precursors, a 2D heterogeneous model is

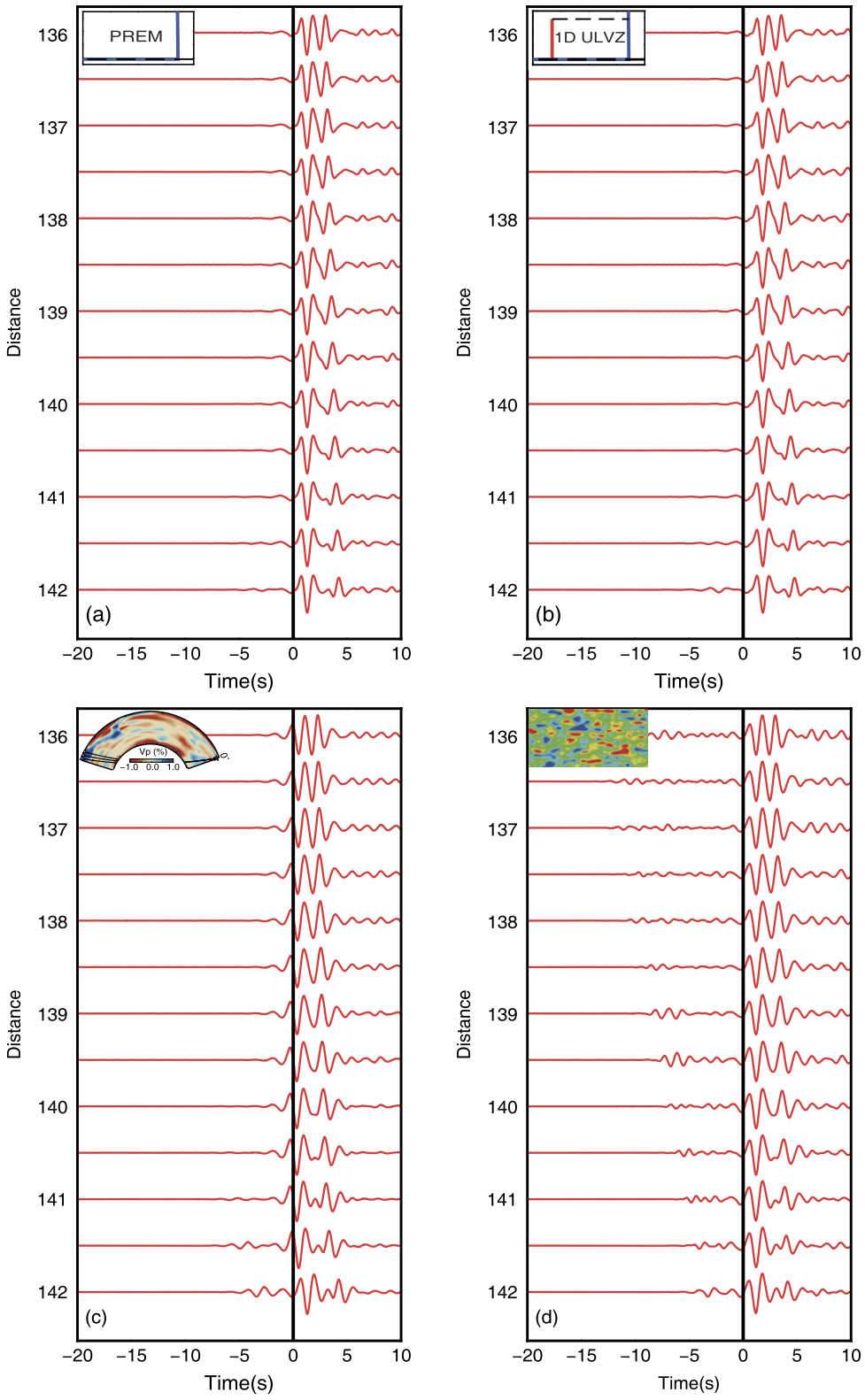


**Fig. 7.** Synthetic waveforms for PREM (Dziewonski and Anderson, 1981) (a), a 1D ULVZ model with thickness of 30 km and P-wave velocity reduction of 10% (b), a long wavelength heterogeneity model (c), and a random heterogeneity model (d). The models are plotted on the top left corner of each panel. The model in panel (c) is the cross section of GyPSuM (Simmons et al., 2010) tomographic model along our earthquake-station great-circle path. The model in panel (d) is a model with random scatterers distributed within 300 km above the CMB. The maximum P-wave perturbation is 2%. Except the PKP b-caustic diffractions, the PREM and 1D ULVZ model do not generate PKP precursors and the long wavelength model shows no obvious precursors. In contrast, the small-scale random scatterer model produces random PKP precursors (type 1 in our data).

thus needed. Further tests show that a model with negative velocity variations is required to fit our observed type 2 data. We tested three ULVZ models with different shapes (Fig. S3) and found that at this stage, we are not able to distinguish these shapes, thus for simplicity, we use sinusoid-shaped model in the following modeling.

Since PKP precursors are generally not sensitive to shear wave and density variations (Fig. S4), in the waveform synthetic process, we only varied P-wave velocity (up to 10% reduction), thickness (10–100 km), and width (20 km to several hundreds of kms) of ULVZ models and compared the synthetic waveforms with the observations. In the modeling, we set our ULVZ models with shear wave reduction of 30% and density increase of 10%, which are generally the case for most of the ULVZs (Garnero and Helmberger, 1998; Rost et al., 2006; Yu and Garnero, 2018). Our tests show that, firstly, there are trade-offs between the ULVZ volume and velocity reduction. For example, a 30 km thick, 30 km wide ULVZ with −10% Vp variation can generate similar precursors as a 60 km thick, 60 km wide ULVZ with −3% Vp variation for the distance range between 138° and 143° (Fig. S5). Secondly, the width of the ULVZ structure does have some effects on the precursors, in that the wide ULVZ can produce two precursor phases interfering with each other (Fig. S6). The trade-offs between the volume and velocity variations could possibly be resolved by the Monte Carlo inversion process, which is, however, beyond the scope of this paper.

We further tested two isolated small-scale ULVZ structures and found that they can also generate two precursor phases (Fig. S7). These results suggest that PKP precursors arise from the sharp velocity transition on the edge of the ULVZ, which is similar to the results of Vanacore et al. (2010). We also notice that it is difficult to image exactly where the later PKP precursors are from, since they could be due to multiple scattering or different small-scale scatterers. Thus we only model the first PKP precursor phase in our study.

Considering the following facts, 2D small-scale ULVZs are preferred in our final model. (1) The coherent type 2 PKP precursors can only be observed at short period waveforms and the size of scatterer should be comparable with the wavelength of seismic wave; (2) the close distribution of type 1 and type 2 PKP precursors in the study region suggests that the ULVZ structures should not have large dimensions but be relatively small.

Our preferred models are small-scale ULVZs with P-wave velocity reductions of 6–10%, thicknesses ranging from 20 km to 30 km and widths of ∼30 km at the CMB. The velocity reduction and size of these ULVZs are similar to previous studies (Wen and Helmberger, 1998; Rost et al., 2005). The synthetic and observed seismograms, together with the ULVZ models, are plotted in Fig. 8. PKIKP is set as reference phase here, since the raypath of it is close to that of PKP precursor above the CMB. We also display the locations of these modeled ULVZs on Fig. 6. It is clear that these locations correlate well with the strong scattering regions on the CMB (blue areas). This consistency thus proves that the ULVZs along the eastern Pacific boundary are the cause of the coherent PKP precursors.

## 5. Discussion

Our small-scale ULVZ structure on the eastern side of the Pacific LLSVP are quite unique compared with previous P-wave studies. As we pointed out, 2D ULVZ structures are required in explaining our data, since a 1D model cannot generate the PKP precursors observed. Wen and Helmberger (1998) and Vanacore et al. (2010) explored 2D ULVZ structures using PKP precursor data as well. Their studies share some similarities with ours, especially in P-wave velocity changes. However, their results are on a much larger scale, and they do not explore lateral variations of the ULVZ, since the data they used are quite limited in space. Our results, on the other hand, reveal more complex structures with small-scale ULVZs surrounded by random heterogeneities.

We notice that, although we prefer small-scale ULVZ structures to explain our data, there are other factors that may also need to be considered, as discussed below.

### 5.1. Factors affecting numerical results

The relative amplitude between PKP precursors and PKIKP phases can be affected by inner core attenuation ($Q_\alpha$ value) (Waszek et al., 2015), and improper use of small $Q_\alpha$ may cause the ratio to be larger. Previous studies suggest that $Q_\alpha$ values in the inner core vary from ∼150 to 1000, and are different in the western and eastern hemisphere (Attanayake et al., 2014; Pejić et al., 2017). However, all of our data are equatorial data that fall into the western hemisphere in the inner core (Fig. 2). Based on previous results, $Q_\alpha$ in equatorial directions in the western inner core ranges from ∼300 to 620, although results from Pejić et al. (2017) show anomalously low $Q_\alpha$ at around 200 in the corresponding region. However, the study of Pejić et al. (2017) includes few data in the region for inversion and has large uncertainties.

To test the effects of inner core structure on the relative amplitude ratios, we calculated the synthetic waveforms based on different attenuation values. Our results show that except for extremely low attenuation (e.g., $Q = 100$), the modeled PKIKP amplitude would not be strongly affected by inner core attenuation (Fig. S8). For a 300-km deep earthquake that is recorded at a distance of 141°, the PKIKP amplitude ratio for different $Q_\alpha$ (620 and 300) is only about 1.3. In the simulations, we set the $Q_\alpha$ value of the inner core to be 360, which is a proper estimation.

Besides the inner core attenuation, the topography of the CMB could also affect the scattered PKP precursors (Doornbos, 1978). At scales of tens to several hundreds of kms, the CMB topography is generally believed to be less than 5 km (e.g., Sze and van der Hilst, 2003; Tanaka, 2010). Although a 5 km topography of the CMB could produce the PKP precursor as well (Fig. S9), we exclude this possibility, because, first, for such large topography, the dominant frequency of precursors would be higher than 2.0 Hz, considering the wavelength of scattered waves should be compatible with the undulation of the CMB topography (Vanacore et al., 2010). However, in our study, most of the PKP precursors are visible at frequency range of 0.5–2.0 Hz, which suggests that the topography needs to be larger than 6 km. Moreover, such topography of the CMB is incompatible with CMB dynamics (Wen, 2000), and thus could not be the reason for our observations. Finally, the relative large amplitude ratios of precursors over PKIKP should not be caused by strong scattering in the lithosphere (Mancinelli and Shearer, 2013), because the depths of selected earthquakes in our case are all larger than 100 km (Table 1), and this effect should be negligible.

### 5.2. Geodynamic implications

High-resolution geodynamical simulations have demonstrated that ULVZs preferentially reside at the boundary of large-scale thermochemical piles, namely LLSVP (McNamara et al., 2010; Li et al., 2017). They are most likely ultra-dense compositionally distinct materials, and occur as discontinuous patches. Moreover, different mantle flows may result in ULVZ patches of different sizes and morphologies (Li et al., 2017).

In this study, our data from adjacent earthquakes have demonstrated the complexity of the heterogeneities in the investigation area, in that some show clear coherent PKP precursor phases while others show more random precursor signals. The coherent precursors have been proved to result from isolated ULVZs that are

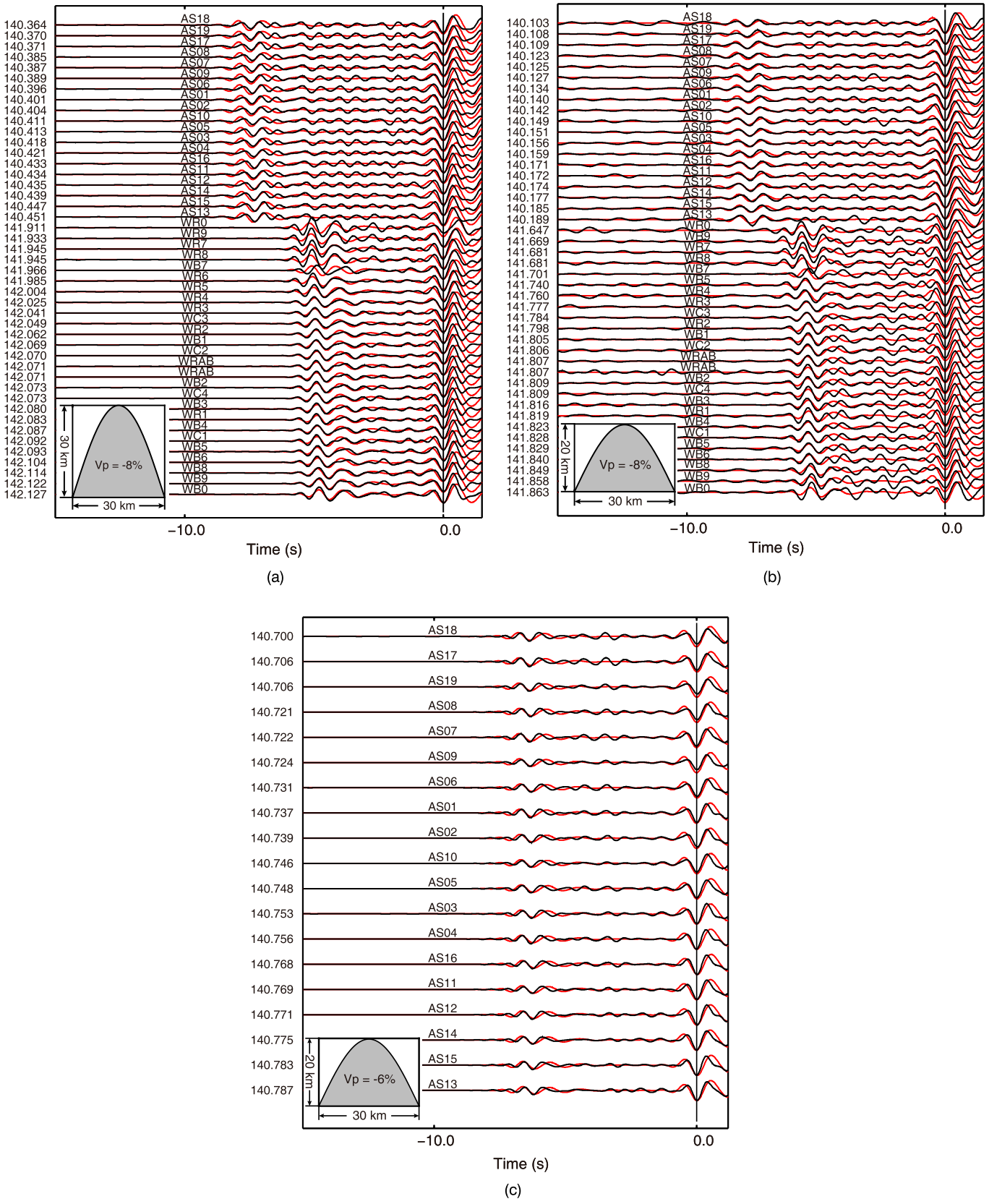


**Fig. 8.** Comparison between synthetic seismograms (red lines) and observed ones (black lines) for three events: (a) 2006.10.31, (b) 2007.07.21, (c) 2010.08.12. All the seismograms are aligned with the peak time of PKIKP phase. ULVZ models used for synthetic waveform modeling are shown in the lower left corner.

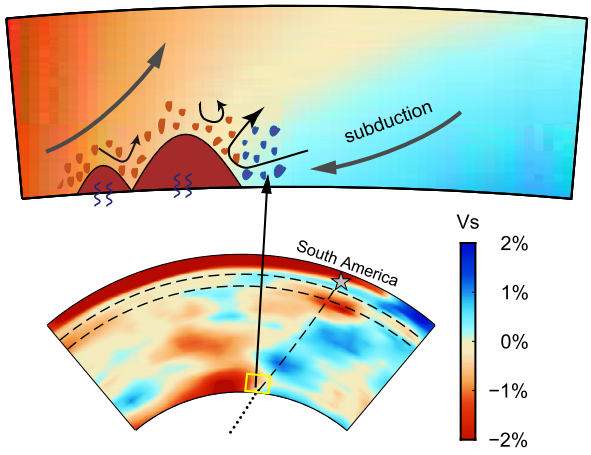


**Fig. 9.** Schematic diagram showing the dynamic process generating ULVZs in the eastern Pacific LLSVP. (Bottom) Cross-section of the great circle between earthquake (gray star) and station (not shown). The background is the shear velocity model from Simmons et al. (2010). The yellow box is the location where our ULVZs are detected. The dashed line represents the ray-path of PKP precursor. (Top) Magnified area of the inserted yellow box in the bottom. The brown sinusoid-shaped structures are ULVZs, and the small brown and blue patches represent random small-scale heterogeneities that generate irregular PKP precursors. The arrows indicate the possible flow directions of mantle convection. The complex flow in this region may be responsible for the isolated ULVZs along the LLSVP boundary.

located along the Pacific LLSVP boundary, whose lateral dimension is several tens of kilometers and heights are from 20 km to 60 km. The random precursors, on the other hand, may be caused by random heterogeneities in between the ULVZs, or multiple heterogeneities at different locations (Fig. S7). This complex pattern indicates vigorous small-scale mantle convections in this region, which is also reflected by the lowermost mantle anisotropy straddling the eastern edge of Pacific LLSVP (Deng et al., 2017). Indeed, the eastern boundary of the Pacific LLSVP has a sharper boundary that transits from slow to fast velocity (He and Wen, 2012; Frost and Rost, 2014). This sharp boundary may be related to the active subducting slabs in the central/south America, which may increase the thermal gradient of the LLSVP boundary, and thus enhance the mechanical mixing of the materials (Fig. 9).

On the other hand, the Galapagos island, a hot spot area, is located to the north of our scattering region (Fig. 6). Tomographic models have revealed a broad upwelling mantle plume that may come from the CMB beneath this area (French and Romanowicz, 2015). Nickel and helium isotope analysis of Galapagos lava suggest that they are from less-degassed nickel-rich melt above the CMB (Herzberg et al., 2013). This melt is then suggested to be related with the mantle–core interaction, through which core materials react with the lower mantle silicate, and produce dense materials that form the observed ULVZs. One possible scenario is that iron droplets from the core could percolate upward into the mantle and react with postperovskite (Sakai et al., 2006) or ferropericlase (Brown et al., 2015). These iron-enriched materials thus provide an explanation for the ULVZs. However, we could not rule out the possibility that the subducted oceanic crust is a source of dense, small-scale compositional ULVZ materials (Christensen and Hofmann, 1994), considering the subducted slabs nearby.

We also notice that the uprising plume may provide a heat source of this region. It may cause partial melting to happen. However, the distribution of isolated ULVZs in such a small dimension is not likely mainly due to the thermal effect, and we believe that compositional differences take the main role in ULVZ formation in the eastern boundary of the Pacific LLSVP.

## 6. Conclusion

Using clear PKP precursors recorded by two Australian arrays (ASAR and WRA) from earthquakes in South America, we have detected heterogeneous scatterers near the CMB along the eastern boundary of the Pacific LLSVP. Our results show that these scatterers are mainly distributed in the localized region (2°S to 25°S in latitude and 80°W to 100°W in longitude) at the CMB. They show complex patterns, with isolated small-scale ULVZs and random heterogeneities in between. Modeling results reveal that the ULVZs in this study are located along the boundary of the Pacific LLSVP, with P-wave velocity reductions of 3–10%, thicknesses ranging from 20 km to 60 km and widths of about several tens of kilometers. Considering the location, dimension and distribution of these ULVZs, together with the subducted slab and upwelling plume nearby, we suggest that the ULVZs are most likely caused by compositionally distinct materials from either core–mantle reaction, or subducted slabs, although partial melting may also exist. The distribution of small-scale ULVZs also implies more complex, localized mantle convections in the lowermost mantle, which may be related to the active subduction and upwelling nearby.

High frequency PKP precursors are shown to provide an alternative approach to exploring the ULVZ regions that are inaccessible by reflected or diffracted phases. However, in this study, we could not place tighter constraints on the density variation of ULVZ, because PKP precursors are not very sensitive to it. The limited distribution of seismic stations hinders our complete imaging of the whole ULVZ structure in this region. Multiple seismic probes, such as converted phases (such as ScP, PcS), or more data coverage in the same regions, are needed in the future.

## Acknowledgements

We would like to thank three reviewers and the editor for their constructive comments, which help improve the manuscript. This work is supported by the National Science Foundation of China (No. 41774053), the Strategic Priority Research Program (B) of Chinese Academy of Sciences (Grant No. XDB18000000), and Special Program for Applied Research on Super Computation of the NSFC–Guangdong Joint Fund. XM has been supported by the Sino-German (CSC-DAAD) Postdoc Scholarship Program during the research (No. 57343410). Discussions with D. Sun were helpful in preparing the manuscript. Figures are made using Generic Mapping Tools (Wessel and Smith, 1998). The AxiSEM program is conducted on Milkyway-II supercomputer clusters of Super Computation Center in Guangzhou. All seismic data are available from IRIS website. The facilities of IRIS Data Services, and specifically the IRIS Data Management Center, were used for access to waveforms, related metadata, and/or derived products used in this study.

## Appendix A. Supplementary material

Supplementary material related to this article can be found online at https://doi.org/10.1016/j.epsl.2018.11.037.

## References

Attanayake, J., Cormier, V.F., de Silva, S.M., 2014. Uppermost inner core seismic structure – new insights from body waveform inversion. Earth Planet. Sci. Lett. 385, 49–58.

Berryman, J.G., 2000. Seismic velocity decrement ratios for regions of partial melt in the lower mantle. Geophys. Res. Lett. 27, 421–424.

Brown, S.P., Thorne, M.S., Miyagi, L., Rost, S., 2015. A compositional origin to ultralow-velocity zones. Geophys. Res. Lett. 42, 1039–1045.

Cao, A., Romanowicz, B., 2007. Locating scatterers in the mantle using array analysis of PKP precursors from an earthquake doublet. Earth Planet. Sci. Lett. 255, 22–31.

Christensen, U.R., Hofmann, W., 1994. Segregation of subducted oceanic crust in the convecting mantle. J. Geophys. Res., Solid Earth 99, 19867–19884.
Cottaar, S., Romanowicz, B., 2012. An unusually large ULVZ at the base of the mantle near Hawaii. Earth Planet. Sci. Lett. 355–356, 213–222.
Deng, J., Long, M.D., Creasy, N., Wagner, L., Beck, S., Zandt, G., Tavera, H., Minaya, E., 2017. Lowermost mantle anisotropy near the eastern edge of the Pacific LLSVP: constraints from SKS–SKKS splitting intensity measurements. Geophys. J. Int. 210, 774–786.
Doornbos, D.J., 1978. On seismic-wave scattering by a rough core–mantle boundary. Geophys. J. R. Astron. Soc. 53, 643–662.
Dziewonski, A.M., Anderson, D.L., 1981. Preliminary reference Earth model. Phys. Earth Planet. Inter. 25, 297–356.
French, S.W., Romanowicz, B., 2015. Broad plumes rooted at the base of the Earth's mantle beneath major hotspots. Nature 525, 95–99.
Frost, D.A., Rost, S., 2014. The P-wave boundary of the large-low shear velocity province beneath the Pacific. Earth Planet. Sci. Lett. 403, 380–392.
Garnero, E.J., Helmberger, E.J., 1998. Further structural constraints and uncertainties of a thin laterally varying ultralow-velocity layer at the base of the mantle. J. Geophys. Res., Solid Earth 103, 12495–12509.
Garnero, E.J., McNamara, A., Shim, S-H., 2016. Continent-sized anomalous zones with low seismic velocity at the base of Earth's mantle. Nat. Geosci. 9, 481–489.
He, Y., Wen, L., 2012. Geographic boundary of the "Pacific Anomaly" and its geometry and transitional structure in the north. J. Geophys. Res., Solid Earth 117, B09308.
Hedlin, M.A.H., Shearer, P.M., Earle, P.S., 1997. Seismic evidence for small-scale heterogeneity throughout Earth's mantle. Nature 387, 145–150.
Hernlund, J.W., Tackley, P.J., 2007. Some dynamical consequences of partial melting in Earth's deep mantle. Phys. Earth Planet. Inter. 1–2, 149–163.
Herzberg, C., Asimow, P.D., Ionov, D.A., Vidito, C., Jackson, M.G., Geist, D., 2013. Nickel and helium evidence for melt above the core–mantle boundary. Nature 493, 393–397.
Kaneshima, S., 2013. Lower mantle seismic scatterers below the subducting Tonga slab: evidence for slab entrainment of transition zone materials. Phys. Earth Planet. Inter. 222, 35–46.
Lay, T., Garnero, E.J., 2011. Deep mantle seismic modeling and imaging. Annu. Rev. Earth Planet. Sci. 39, 91–123.
Li, M., McNamara, A.K., Garnero, E.J., Yu, S., 2017. Compositionally-distinct ultra-low velocity zones on Earth's core–mantle boundary. Nat. Commun. 8, 177.
Mancinelli, N.J., Shearer, P.M., 2013. Reconciling discrepancies among estimates of small-scale mantle heterogeneity from PKP precursors. Geophys. J. Int. 195, 1721–1729.
McNamara, A.K., Garnero, E.J., Rost, S., 2010. Tracking deep mantle reservoirs with ultra-low velocity zones. Earth Planet. Sci. Lett. 299, 1–9.
Miller, M.S., Niu, F., 2008. Bulldozing the core–mantle boundary: localized seismic scatterers beneath the Caribbean Sea. Phys. Earth Planet. Inter. 170, 89–94.
Mori, J., Helmberger, D.V., 1995. Localized boundary layer below the mid-Pacific velocity anomaly identified from a PcP precursor. J. Geophys. Res., Solid Earth 100, 20359–20365.
Nissen-Meyer, T., van Driel, M., Stähler, S.C., Hosseini, K., Hempel, S., Auer, L., Colombi, A., Fournier, A., 2014. AxiSEM: broadband 3-D seismic wavefields in axisymmetric media. Solid Earth 5, 425–445.
Pejić, T., Tkalčić, H., Sambridge, M., Cormier, V.F., Benavente, R., 2017. Attenuation tomography of the upper inner core. J. Geophys. Res., Solid Earth 122, 3008–3032.
Rost, S., Garnero, E.J., Williams, Q., Manga, M., 2005. Seismological constraints on a possible plume root at the core–mantle boundary. Nature 435, 666–669.
Rost, S., Garnero, E.J., Williams, Q., 2006. Fine-scale ultralow-velocity zone structure from high-frequency seismic array data. J. Geophys. Res., Solid Earth 111, B09310.
Rost, S., Thomas, C., 2002. Array seismology: methods and applications. Rev. Geophys. 40, 1008.
Sakai, T., Kondo, T., Ohtani, E., Terasaki, H., Endo, N., Kuba, T., Suzuki, T., Kikegawa, T., 2006. Interaction between iron and post-perovskite at core–mantle boundary and core signature in plume source region. Geophys. Res. Lett. 33, L15317.
Simmons, N.A., Forte, A.M., Boschi, L., Grand, S.P., 2010. GyPSuM: a joint tomographic model of mantle density and seismic wave speeds. J. Geophys. Res., Solid Earth 115, B12310.
Sze, E.K.M., van der Hilst, R.D., 2003. Core mantle boundary topography from short period PcP, PKP and PKKP data. Phys. Earth Planet. Inter. 135, 27–46.
Tackley, P.J., 2012. Dynamics and evolution of the deep mantle resulting from thermal, chemical, phase and melting effects. Earth-Sci. Rev. 110, 1–25.
Tanaka, S., 2010. Constraints on the core–mantle boundary topography from P4KP-PcP differential travel times. J. Geophys. Res., Solid Earth 115, B04310.
Thomas, C., Kendall, J.M., Helffrich, G., 2009. Probing two low-velocity regions with PKP b-caustic amplitudes and scattering. Geophys. J. Int. 178, 503–512.
Thomas, C., Weber, M., Wicks, C.W., Scherbaum, F., 1999. Small scatterers in the lower mantle observed at German broadband arrays. J. Geophys. Res., Solid Earth 104, 15073–15088.
Thorne, M.S., Garnero, E.J., 2004. Inferences on ultralow-velocity zone structure from a global analysis of SPdKS waves. J. Geophys. Res., Solid Earth 109, B08301.
Thorne, M.S., Garnero, E.J., Jahnke, G., Igel, H., McNamara, A.K., 2013. Mega ultra low velocity zone and mantle flow. Earth Planet. Sci. Lett. 364, 59–67.
Vanacore, E., Niu, F., Ma, Y., 2010. Large angle reflection from a dipping structure recorded as a PKP precursor: evidence for a low velocity zone at the core–mantle boundary beneath the Gulf of Mexico. Earth Planet. Sci. Lett. 293, 54–62.
Vidale, J.E., Hedlin, M.A.H., 1998. Evidence for partial melt at the core–mantle boundary north of Tonga from the strong scattering of seismic waves. Nature 391, 682–685.
Waszek, L., Thomas, C., Deuss, A., 2015. PKP precursor: implications for global scatterers. Geophys. Res. Lett. 42, 3829–3838.
Wen, L., 2000. Intense seismic scattering near the core–mantle boundary beneath the Comoros hotspot. Geophys. Res. Lett. 27, 3627–3630.
Wen, L., Helmberger, D.V., 1998. Ultra low velocity zones near the core–mantle boundary from broadband PKP precursors. Science 279, 1701–1703.
Wessel, P., Smith, W.H.F., 1998. New improved version of Generic Mapping Tools released. EOS, Trans. Am. Geophys. Un. 79, 579.
Williams, Q., Garnero, E.J., 1996. Seismic evidence for partial melt at the base of the Earth's mantle. Science 273, 1528–1530.
Williams, Q., Revenaugh, J., Garnero, E.J., 1998. A correlation between ultra-low basal velocities in the mantle and hot spots. Science 281, 546–549.
Yao, J., Wen, L., 2014. Seismic structure and ultra-low velocity zones at the base of the Earth's mantle beneath Southeast Asia. Phys. Earth Planet. Inter. 233, 103–111.
Yu, S., Garnero, E.J., 2018. Ultralow velocity zone locations: a global assessment. Geochem. Geophys. Geosyst. 19, 396–414.
Yuan, K., Romanowicz, B., 2017. Seismic evidence for partial melting at the root of major hot spot plumes. Science 357, 1–5.
Zhao, C., Garnero, E.J., Li, M., McNamara, A., Yu, S., 2017. Intermittent and lateral varying ULVZ structure at the northeastern margin of the Pacific LLSVP. J. Geophys. Res., Solid Earth 122, 1198–1220.